Neuronal control of astrocytic respiration through a variant of the Crabtree effect

Ignacio Fernández-Moncada[a,b], Iván Ruminot[a,c], Daniel Robles-Maldonado[a,b], Karin Alegría[a], Joachim W. Deitmer[c], and L. Felipe Barros[a,1]

[a]Centro de Estudios Científicos, 5110466 Valdivia, Chile; [b]Universidad Austral de Chile, 5110566 Valdivia, Chile; and [c]Department of Biology, Division of General Zoology, University of Kaiserslautern, D-67653 Kaiserslautern, Germany

Edited by Marcus E. Raichle, Washington University in St. Louis, St. Louis, MO, and approved December 28, 2017 (received for review September 18, 2017)

Aerobic glycolysis is a phenomenon that in the long term contributes to synaptic formation and growth, is reduced by normal aging, and correlates with amyloid beta deposition. Aerobic glycolysis starts within seconds of neural activity and it is not obvious why energetic efficiency should be compromised precisely when energy demand is highest. Using genetically encoded FRET nanosensors and real-time oxygen measurements in culture and in hippocampal slices, we show here that astrocytes respond to physiological extracellular K^+ with an acute rise in cytosolic ATP and a parallel inhibition of oxygen consumption, explained by glycolytic stimulation via the Na^+-bicarbonate cotransporter NBCe1. This control of mitochondrial respiration via glycolysis modulation is reminiscent of a phenomenon previously described in proliferating cells, known as the Crabtree effect. Fast brain aerobic glycolysis may be interpreted as a strategy whereby neurons manipulate neighboring astrocytes to obtain oxygen, thus maximizing information processing.

potassium | NBCe1 | aerobic glycolysis | ATP | oxygen

Cellular energy balance is explained by feedback mechanisms that respond to ATP depletion through stimulation of mitochondrial oxidative phosphorylation (OXPHOS) and glycolysis (1). An example operates in astrocytes, in which the activation of the Na^+/K^+ ATPase pump by glutamate and K^+ stimulates glycolysis in response to neuronal activity (2, 3). To characterize the energetic mechanisms involved in the early adaptation of astrocytic homeostasis to workload, we monitored astrocytic ATP in organotypic hippocampal slices with the genetically encoded FRET nanosensor ATeam 1.03 (4). Surprisingly, synaptic activity induced by Schaeffer collateral stimulation provoked an ATP rise instead of ATP depletion (Fig. 1*A* and *SI Appendix*, Fig. S1). The response was fast and quickly reversed upon cessation of the stimuli. Excitatory synaptic activity releases glutamate and K^+, which are promptly cleared by neighboring astrocytes. To assess the relative contribution of these signals to the ATP rise, we studied astrocytes in coculture with neurons, where they maintain their metabolic differentiation (5, 6). Exposure to elevated extracellular potassium $\{[K^+]_e\}$ effectively mimicked the ATP increase observed in tissue slices (Fig. 1 *B* and *C* and *SI Appendix*, Fig. S2), but application of glutamate led to the opposite change (Fig. 1 *B* and *C*). The response of ATP to $[K^+]_e$ displayed a half saturation constant of 3.6 mM (Fig. 1*D* and *SI Appendix*, Fig. S2), which is within the range present in brain interstitium under physiological conditions (7). It was unaffected by blockage of OXPHOS and it was abolished by inhibition of glycolysis (Fig. 1*E* and *SI Appendix*, Fig. S3) evidencing up-regulated glycolytic ATP production. A recently identified mechanism for fast glycolysis modulation in astrocytes is mediated by $[K^+]_e$ through the Na^+-bicarbonate cotransporter NBCe1 (Fig. 1*F*) (3, 8–10). Consistent with a major role for this pathway, the ATP rise was significantly smaller in astrocytes from NBCe1 knockout mice, both in culture and in hippocampal slices, and it was inhibited by the NBCe1 blocker S0859 (Fig. 1 *G* and *H* and *SI Appendix*, Fig. S4). The delayed ATP increase remaining in the knockout mice may correspond to an additional, slower mechanism of glycolytic activation by $[K^+]_e$ or to some form of compensation. K^+ stimulation of a cell line lacking endogenous NBCe1 activity (8) also led to ATP depletion, as expected from Na^+ pump engagement (*SI Appendix*, Fig. S4). These results indicate that glycolytic production of ATP commanded by $[K^+]_e$ via the NBCe1 surpasses the usage of ATP by the Na^+ pump, jointly stimulated by glutamate (through intracellular Na^+) and $[K^+]_e$.

ATP and its hydrolysis product ADP are major controllers of mitochondrial respiration (1, 11, 12) and have been linked to the inhibition of mitochondrial oxygen consumption in response to glycolytic flux, a phenomenon termed the Crabtree effect (13–15). A first indication of mitochondrial modulation was the accumulation of cytosolic pyruvate in K^+-stimulated astrocytes, explained by reduced pyruvate consumption (Fig. 2 *A* and *B* and *SI Appendix*, Fig. S5). Next, we developed a methodology based on oxygen-quenching lifetime fluorescence and a high-surface 3D-printed coverslip (Fig. 2*C* and *SI Appendix*, Figs. S6 and S7), which allowed real-time measurement of oxygen consumption by adherent cells in the presence of physiological bicarbonate (Fig. 2 *D* and *E*). Using this approach, astrocytes were found to respond to high $[K^+]_e$ with substantial inhibition of oxygen consumption (Fig. 2*F*). Consistent with a major role for NBCe1 and its fast activation of glycolysis, the effect of high $[K^+]_e$ on respiration was inhibited by S0859 (Fig. 2*G*) and could be detected within seconds of exposure to high $[K^+]_e$ (Fig. 2*H* and *SI Appendix*, Fig. S8).

To assess the impact of the phenomenon in brain tissue, local oxygen levels were measured in hippocampal slices with a microelectrode (*SI Appendix*, Fig. S9). In response to high $[K^+]_e$ there was a rapid and reversible decrease in local oxygen (Fig. 3 *A* and *B*), consistent with increased neuronal oxygen consumption. Significantly, stimulation of the same slice in the presence of TTX, resulted in an increase in local oxygen, demonstrative of reduced consumption (Fig. 3 *A* and *B*). As TTX diminishes neuronal activity and the other major oxygen consumer in gray matter is the astrocyte, we ascribed the oxygen rise in the presence

Significance

Neuronal activity is immediately followed by aerobic glycolysis, the partial oxidation of glucose to lactate in the presence of oxygen, a phenomenon that seems paradoxical because full oxidation of glucose to CO_2 would yield much more ATP. Here we show that short-term aerobic glycolysis involves a mechanism whereby neurons obtain oxygen by manipulating the glucose metabolism and mitochondrial respiration of neighboring astrocytes.

Author contributions: I.F.-M., I.R., and L.F.B. designed research; I.F.-M., I.R., D.R.-M., K.A., and L.F.B. performed research; J.W.D. contributed new reagents/analytic tools; I.F.-M., I.R., D.R.-M., J.W.D., and L.F.B. analyzed data; and I.F.-M. and L.F.B. wrote the paper.

The authors declare no conflict of interest.

This article is a PNAS Direct Submission.

[1]To whom correspondence should be addressed. Email: fbarros@cecs.cl.

This article contains supporting information online at www.pnas.org/lookup/suppl/doi:10.1073/pnas.1716469115/-/DCSupplemental.

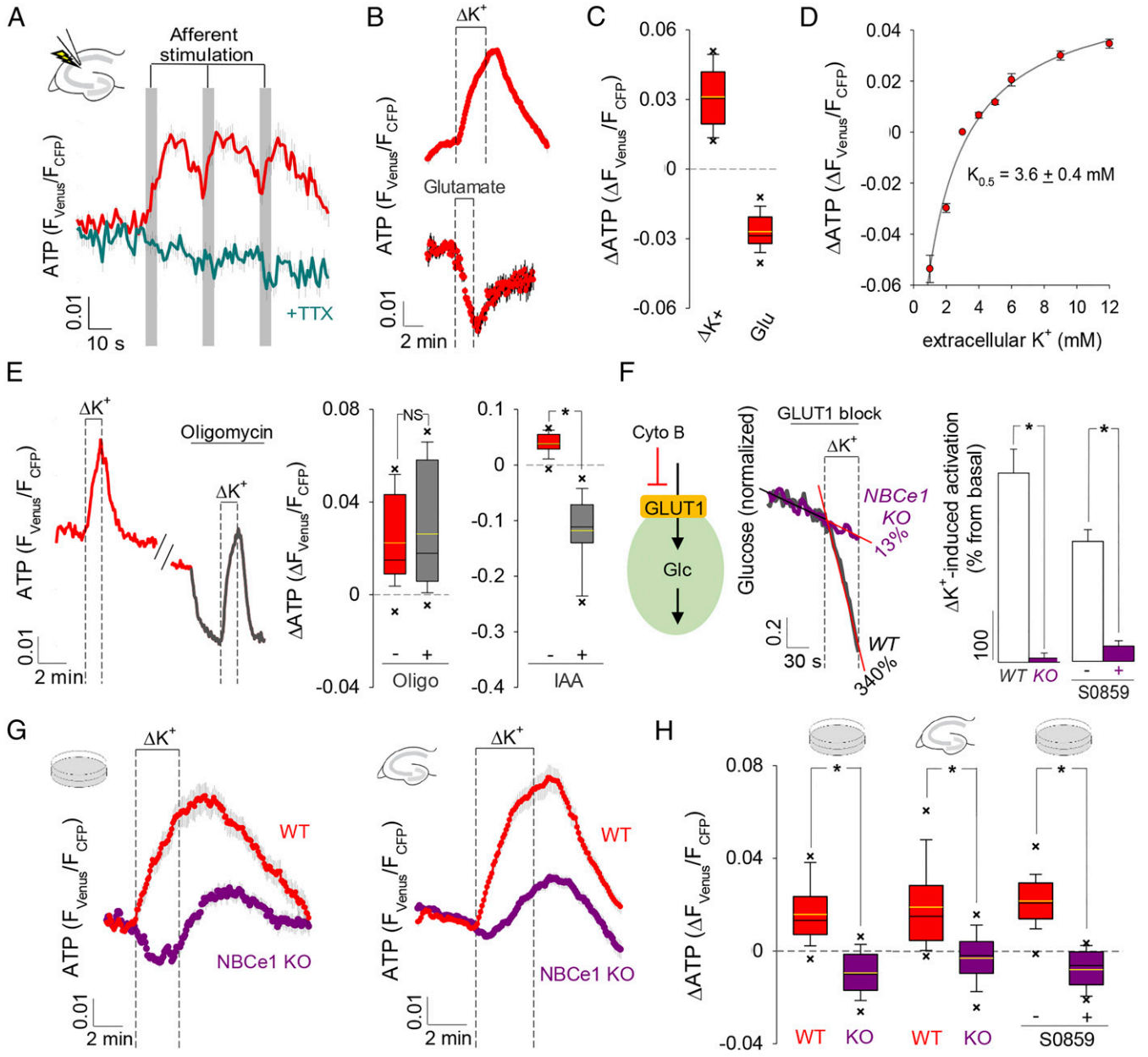

Fig. 1. Astrocytic ATP increase mediated by the NBCe1 and glycolysis. (*A*) ATP during evoked synaptic activity in the absence and presence of 0.5 μM TTX, n = 3, 48 cells. (*B*) Response of ATP to a rise from 3 to 12 mM K^+ (ΔK^+; n = 7, 60 cells) and to exposure to 50 μM glutamate (n = 3, 27 cells). (*C*) Summary of ATP changes induced by ΔK^+ and glutamate (Glu) shown in *B*. (*D*) Effect of K^+ decreases and increases on ATP (n = 3, 24 cells). (*E*, *Left*) ATP in a cell exposed to ΔK^+ in the absence and presence of 2.5 μM oligomycin (oligo). (*E*, *Right*) Summary of three similar experiments (19 cells) and of analogous experiments with 500 μM iodoacetic acid (IAA, 30 min, n = 3, 25 cells). NS, nonsignificant. (*F*) Glucose consumption rate was measured before and after ΔK^+ exposure by blocking GLUT1 with cytochalasin B (20 μM), in wild type (WT, n = 2, 10 cells) and NBCe1 KO astrocytes (n = 3, 15 cells), or in the absence and presence of 30 μM S0859 (n = 3, 36 cells). Rate stimulations were 340% for WT and 13% for NBCe1 KO. (*G*) ΔK^+-mediated ATP responses in NBCe1 KO (culture, n = 6, 54 cells; slices, n = 12, 117 cells) and WT astrocytes (culture, n = 3, 27 cells; slices, n = 6, 68 cells). (*H*) Summary of the experiments in *G* and of analogous experiments with cultured astrocytes in the absence and presence of 30 μM S0859 (n = 3, 23 cells). *P < 0.05.

of TTX to astrocytes. A mathematical simulation (*SI Appendix*) serves to illustrate how graded inhibition of astrocytic respiration would counteract the depletion of tissue oxygen during neural activity, therefore increasing the availability of oxygen to neurons (Fig. 3*C* and *SI Appendix*, Fig. S10).

Neural activity is accompanied by local stimulation of glycolysis in excess of oxygen consumption, a phenomenon termed aerobic glycolysis (16, 17), which supports synapse formation and growth (18), is reduced during normal aging (19), and shows spatial correlation with Alzheimer's disease amyloid beta deposition (20). The presence of aerobic glycolysis in brain tissue immediately after activity, that is, when ATP demand is maximum, is counterintuitive, because full glucose oxidation in mitochondria would generate 15 times more ATP. Our data suggest that quick aerobic glycolysis is mediated by K^+ stimulation of astrocytic NBCe1 and that its physiological role is to spare oxygen for neuronal usage (Fig. 3*D*).

Suppression of respiration secondary to glycolytic flux, the Crabtree effect, has been described in yeast, cancer cells, and other proliferating cells (14, 15). The phenomenon reported here may be seen as a variety of the Crabtree effect in which respiration

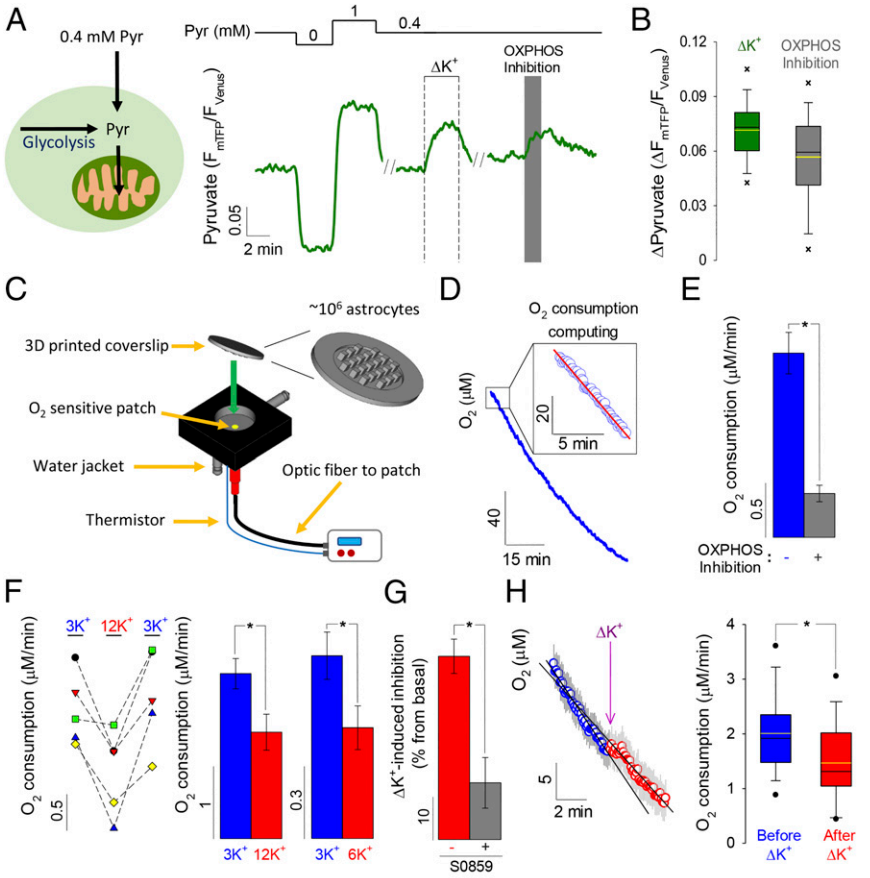

Fig. 2. Astrocytic O_2 consumption inhibition mediated by the NBCe1. (*A*) Single-cell pyruvate changes in response to high K^+, measured in 0.4 mM extracellular pyruvate for maximal sensitivity to mitochondrial perturbation (47). OXPHOS was inhibited with 5 mM azide. (*B*) Summary of the pyruvate increases induced by high K^+ and OXPHOS inhibition ($n = 6$, 51 cells). (*C*) Device to monitor real-time respiration in adherent cells, based on an O_2-sensitive patch within a chamber sealed with a high-surface 3D-printed coverslip. (*D*) O_2 consumption is computed as the rate of oxygen decrease soon after sealing of the chamber (*Inset*). (*E*) Effect of OXPHOS inhibition with 5 mM sodium azide on astrocytic oxygen consumption ($n = 16$). (*F*, *Left*) O_2 consumption measured before, during, and after exposure to 12 mM K^+ ($n = 5$). (*F*, *Right*) Summary of the effects of 12 and 6 mM K^+ ($n = 5$). (*G*) Inhibition induced by 12 mM K^+, in the absence and presence of 30 μM S0859 ($n = 5$). (*H*) Acute effect of 12 mM K^+ on O_2 consumption achieved by KCl injection into the sealed chamber ($n = 15$). *$P < 0.05$.

is not inhibited by the availability of glucose but by an external signal that speeds up glycolysis. Astrocytes have a very high resting K^+ permeability that renders their membrane potential exquisitely sensitive to $[K^+]_e$. At rest $[K^+]_e$ is ∼2.5–3 mM, which translates into an astrocytic membrane potential of about −80 mV, close to the equilibrium potential of the NBCe1. Active neurons release K^+ via ionotropic receptors and K^+-selective channels causing high $[K^+]_e$, astrocytic depolarization, and influx of bicarbonate through the NBCe1 (21–24). The resulting cytosolic alkalinization stimulates astrocytic glycolysis (3, 8–10), inducing an acute Crabtree effect by multiple parallel mechanisms operating on OXPHOS complexes, including ADP inhibition of the F_1F_0 ATP synthase (1, 11, 25), inhibition of complex IV by ATP (12), and inhibition of complexes III and IV by reciprocal changes in fructose-1,6-bisphosphate and glucose-6-phosphate (15).

Astrocytes appear particularly well equipped for the Crabtree effect as they have a vast glycolytic capacity conferred by PFKFB3, the master regulator of the pathway (6, 26). Strikingly, this capacity allows them to withstand pharmacological and genetic ablation of OXPHOS, which is not the case for neurons (27, 28). Astrocytes also possess a much higher fraction of deactive complex I than neurons (29), which echoes the evolutionary loss of complex I that preceded the emergence of the Crabtree effect in yeast (30). We wonder whether deactive complex I in astrocytes may contribute to the K^+-induced Crabtree effect and perhaps also to the response of these cells to nitric oxide, another signal involved in neurometabolic coupling (27, 31, 32). Whereas both K^+ and NO signaling rely on strong glycolysis, in the case of K^+ the primary target is the glycolytic machinery, whereas for NO, the primary target is OXPHOS. The extent of the oxygen redistribution triggered by K^+ and NO will primarily be determined by the relative contribution of astrocytes and neurons to tissue oxygen consumption under resting condition, which is unknown. In vivo MRS has shown that astrocytes account for 20–30% of tissue TCA cycle flux in the awake brain (33–36). Because of their housekeeping roles (37), astrocytes are likely to spend more ATP than neurons under resting conditions and therefore their share of the resting tissue respiration may be even higher, particularly in gray matter where the volume fraction of astrocytes is highest. Thus, the redistribution of oxygen is not just from astrocytes to neurons, but also from housekeeping to signaling. Furthermore, K^+ spreads over a larger area than glutamate (7), meaning that oxygen is likely recruited from regions beyond the active zone. The metabolic effects of K^+ and NO, and also of NH_4^+ (38), three intercellular signals that target astrocytic mitochondria but differ in origin, reach, and time course, highlight the emerging role of glial respiratory inhibition, acting in parallel with functional hyperemia (39, 40) to provide oxygen to neurons.

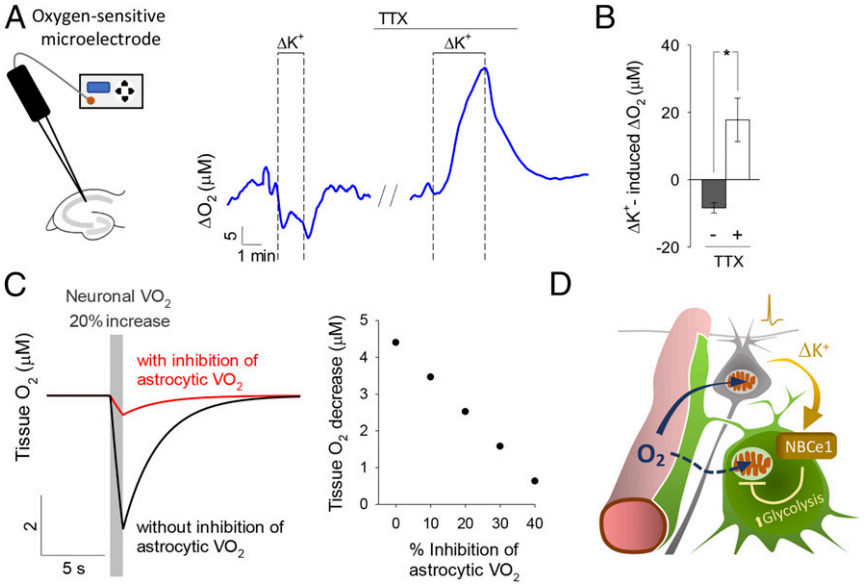

Fig. 3. Local increase in O_2 concentration induced by high $[K^+]_e$. (*A*) The effect of high K^+ (12 mM) on hippocampal tissue O_2 was measured before and during blockage of neuronal activity with 1 μM TTX ($n = 3$). (*B*) Summary of three similar experiments. *$P < 0.05$. (*C*) Numerical simulation of brain tissue O_2 level. (*Left*) Tissue oxygen during a 20% stimulation in neuronal oxygen consumption (VO_2), with astrocytic VO_2 unchanged (black) or with astrocytic VO_2 depressed by 40% (red). (*Right*) Incremental protection against tissue oxygen depletion achieved by incremental astrocytic VO_2 inhibition, at a fixed 20% stimulation of neuronal VO_2. (*D*) Proposed redistribution of brain tissue oxygen toward neurons after induction of the Crabtree effect in astrocytes by neuronal K^+.

Information processing is limited by energy production (41), which in the brain is critically dependent on oxygen, whose turnover is 100 times faster than those of glucose and lactate. By supplementing the capacity of the vasculature to deliver oxygen, fast aerobic glycolysis should therefore maximize the capacity of the brain to process information. In the hippocampus, inhibition of intercellular lactate shuttling led to deficient memory formation (42), so we envisage that deficits in fast aerobic glycolysis may lead to similar network dysfunctions. Behavioral studies are not possible in NBCe1 knockout mice, because these animals die from renal acidosis soon after birth (43), a problem that may be circumvented by inducible NBCe1 deletion. Such an approach should help to investigate whether blockage of fast aerobic glycolysis causes neuronal stress and/or perhaps an adaptive reduction of firing rate, as triggered by hypoxia (44). Addressing this type of questions is important considering the loss of brain aerobic glycolysis during aging (19) and its relationship with degeneration (20). The electrogenic Na^+-bicarbonate cotransporter NBCe1, core of the molecular machinery involved in K^+-induced aerobic glycolysis, is present in mammalian glia (23, 24), in the brain of zebrafish (45), and in the giant glial cell of the leech central nervous system (22), which suggests that activity-dependent glial-neuronal oxygen redistribution may be an evolutionary conserved mechanism.

Material and Methods

Standard chemicals and cell culture reagents were obtained from Sigma. Fluo-4 AM and Magnesium Green AM (acetoxymethyl ester) were obtained from Molecular Probes. Constructs coding for the ATP FRET nanosensor ATeam 1.03 (4), the glucose FRET nanosensor FLII12Pglu700μΔ6 (46), and the pyruvate FRET nanosensor Pyronic (47) have been described previously and are available through Addgene (www.addgene.org). Adenoviral vectors encoding FRET nanosensors were custom made by Vector Biolabs.

Mixed Cortical Brain Cell Cultures. The animals used were mixed F1 male mice (C57BL/6J × CBA/J), kept under specific pathogen-free (SPF) conditions at room temperature (20 ± 2 °C), in a 12-h light/12-h dark cycle with free access to food and water. All experiments were approved by the Centro de Estudios Científicos Animal Care and Use Committee. Mixed cortical cultures of astrocytes and neurons were prepared from 2- to 3-d-old neonatal WT mice (mixed F1 male mice C57BL/6J × CBA/J) or NBCe1A knockout mice (C57BL/6J). Animals were genotyped by PCR (43). Brain was removed and cortex dissected in Hank's medium at 4 °C in sterile conditions. The tissue was enzymatically digested with trypsin/EDTA for 5 min and stopped with 10% FBS in MEM medium at 37 °C. The enzymatically treated tissue was gently dissociated by mechanical force by passing through a 1-mL micropipette tip and cells were left in suspension to allow debris to precipitate. Cells were seeded in 25-mm glass coverslips treated with poly-L-lysine and left for 90 min to allow cell adhesion. After this, medium was replaced with B-27 supplemented neurobasal medium with 10 mM glucose and 2 mM glutamine at 37 °C in a humidified atmosphere of 5% CO_2. At day in vitro (DIV) 7–9, cultures were exposed to 5×10^6 plaque-forming units (pfu) of adenoviral vectors coding for ATeam 1.03, FLII12Pglu700μΔ6, or pyronic. Measurements were carried out 48 h after infection of cells.

Organotypic Hippocampal Slice Preparation. Organotypic hippocampal slice (OHS) preparation was approved by the Landesuntersuchungsamt Rheinland-Pfalz, Koblenz (23 177–07) and by the Centro de Estudios Científicos Animal Care and Use Committee. OHSs from NBCe1 knockout or WT mice were prepared as described (48, 49) with some modifications. In brief, hippocampal slices (400 μm) were cut with a McIlwain tissue chopper (Mickle Laboratory Engineering Company) from 5- to 7-d-old C57BL/6 mice under sterile conditions. Slices were maintained on Biopore membranes (Millicell standing inserts; Merck Millipore) in an interface between humidified normal atmosphere (5% CO_2, 36.5 °C) and culture medium, which consisted of 50% MEM, 25% HBSS, 25% horse serum, and 2 mM L-glutamine and 10 mM D-glucose at pH 7.4 in an incubator (Memmert). The culture medium (1 mL) was replaced three times per week. After 7 d of culture, the slices were transduced by overnight incubation with 5×10^6 pfu of ATeam 1.03 adenoviral vector and imaged after another 4–8 d.

Fluorescence Imaging. Cells were imaged either with an Olympus IX70 inverted fluorescence microscope equipped with a 40× oil-immersion objective (N.A. 1.3), a monochromator and optosplit (Cairn), and a CCD Orca camera (Hamamatsu) controlled by Kinetics software or an Olympus BX50WI upright microscope, equipped with a 20× water immersion objective (N.A. 0.5), monochromator (poly-chrome IV; Till Photonics), optosplit (Cairn), and a cooled CCD camera (Till Photonics). Cultures were mounted in an open chamber and superfused with an imaging solution (in millimoles) of: 10 Hepes, 112 NaCl, 3 KCl, 24 $NaHCO_3$, 1.25 $MgCl_2$, 1.25 $CaCl_2$, 2 glucose, 1 lactate, and bubbled with air/5% CO_2 (pH 7.4) and at room temperature (22–24 °C). Intact Biopore membrane carrying organotypic hippocampal slices were mounted in an open chamber and superfused with an imaging solution (in millimoles) of: 136 NaCl, 3 KCl, 2 $CaCl_2$, 1 $MgCl_2$, 24 $NaHCO_3$, 1.25 NaH_2PO_4, 5 glucose, 1 lactate, and bubbled with air/5% CO_2 (pH 7.4) at

room temperature (22–24 °C). Detailed protocols for the use of the fluorescent sensors for ATP, glucose, and pyruvate are available in detail (4, 46, 47). For FRET measurement, astrocytes expressing a FRET nanosensor were excited at 430 nm for 0.2–0.8 s and the emissions were collected with a 535/15 nm bandpass filter (for Venus and Citrine emission) and a 485/40 nm bandpass filter (for CFP and mTFP emission) and computed as Venus/CFP, Citrine/CFP, and mTFP/Venus ratio for ATeam 1.03, FLII12Pglu700μΔ6 and Pyronic, respectively. For intracellular Mg^{2+} measurements, astrocytes were batch loaded with 5 μM Mg Green AM for 20 min at room temperature. After loading, astrocytes were incubated in imaging solution for 30 min to allow the fluorescent probe deesterification. After this, astrocytes were excited at 490 nm for 0.05–0.15 s and the emission was collected at 535/15 nm. The $1/F_{490}$ was computed and corresponds to an indirect measurement of the ATP level (50, 51). For intracellular Ca^{2+} recording, OHS were batch loaded with the Ca^{2+} sensitive dye Fluo-4 (5 μM) for 30 min at room temperature and excited at 495 nm for 0.05 s and the emission was collected at 535/15 nm. The normalized F_{495} was computed as intracellular Ca^{2+} level. Schaffer collaterals were stimulated using a Grass SD9 stimulator, with train stimulus of 20 Hz for 5 s (40 V) applied to the CA3, and imaging was performed at >200-μm distance from the stimulation area.

Design and Characterization of High Surface Coverslips. The high surface coverslips used to culture astrocytes were designed in a personal computer with FreeCad software (www.freecadweb.org/) and printed using poly-lactic acid (PLA) as material with an Ultimaker 2 3D printer. An astrocyte-enriched culture was obtained by subculture of mixed cortical cultures into the 3D printed high-surface coverslip pretreated with poly-L-lysine. The enriched astrocyte cultures were used after 10–14 d of subculture for the O_2 consumption measurements. For the 3D image reconstruction, astrocytes were batch loaded with 0.5 μM 2′,7′-Bis-(2-carboxyethyl)-5-(and-6)-carboxyfluorescein AM for 5 min at room temperature. A Z-stack series of images (20-μm steps) of a single column of the high-surface coverslip were obtained with an upright Olympus FV1000 confocal microscope equipped with a 10× water immersion objective (N.A. 0.3). Cells were excited with a 488-nm laser and fluorescence was collected at 520 nm. The 3D reconstruction was carried out with the Volume Viewer plugin from ImageJ software (https://imagej.net/).

Oxygen Consumption Measurement. The custom-made device (Instech) to measure oxygen consumption consisted of a small chamber (~200 μL volume) containing an oxygen-sensitive patch, a water jacket, a built-in thermistor, and a bifurcated optic fiber that allow the excitation and measuring of an oxygen-sensitive patch fluorescence (see Fig. 2C for a schematic). The oxygen-sensitive patch corresponds to a sensor based on a fluorescent ruthenium indicator, in a hydrophobic solid-gel matrix, that is quenched as oxygen concentration increases. When excited at 450 nm, the ruthenium complex fluoresces at ~600 nm and is detected by an avalanche photodiode. By pulsing the excitation, the average lifetime fluorescence (τ) can be determined by phase-sensitive detection. A calibration consisting of exposing the oxygen-sensitive patch to N_2 gas (0% O_2) and air/5% CO_2 bubbled buffer (20% O_2) was performed at the start of each measurement. To measure the oxygen consumption, a high surface 3D-printed coverslip cultured with astrocytes was sealed to the device chamber and the oxygen concentration decrease was monitored. A linear fit was computed in the first 5–10 min to obtain the oxygen decrease rate, corresponding to the astrocytic oxygen consumption rate. For experiments of acute increase of extracellular K^+ concentration, a modified high-surface coverslip with an injection port was used (*SI Appendix*, Fig. S9). A volume of 1.8 μL of 1 M KCl was injected with a micropipette through the injection port, obtaining a concentration of ~12 mM K^+ inside the chamber. For control experiments, the same volume of 1 M NaCl was injected. Experiments were carried out at 32–34 °C.

Tissue Oxygen Concentration Measurements. Oxygen concentration in organotypic hippocampal slices was measured with a 10-μm tip diameter Clark-type electrode (Unisense), connected to a digital microsensor amplifier (Unisense), and polarized to −0.8 V for at least 12 h before recordings. To transform the microelectrode signal to oxygen concentration, the microelectrode was calibrated before each experiment by performing a two-point calibration by immersing the microelectrode in a buffer bubbled with N_2/CO_2 (0% oxygen) and air/CO_2 (21% oxygen) at room temperature. For measurements, tissue slices were superfused with 136 NaCl, 3 KCl, 2 $CaCl_2$, 1 $MgCl_2$, 24 $NaHCO_3$, 1.25 NaH_2PO_4, 5 glucose, 1 lactate, and bubbled with air/5% CO_2 (pH 7.4) at room temperature (22–24 °C). All data were collected and transformed to oxygen concentration using SensorTrace software (Unisense).

Statistical Analysis. Regression and statistical analyses were carried out with OriginPro (OriginLab) or Sigma Plot (Systat Software) software. Time courses without error bars correspond to a single cell of a representative experiment. Otherwise, results are presented as mean ± SEM. Data were subjected to a Shapiro–Wilk normality test to choose a parametric (normal distributions) or nonparametric (nonnormal distributions) test. The parametric tests used were either a paired *t* test or two-sample *t* test. Multiple groups were compared using one-way repeated measures ANOVA followed by Tukey's ad hoc test. The nonparametric test used corresponds to a pair sample Wilcoxon signed rank test. A P value <0.05 was considered significant and is indicated with an asterisk (*). Nonsignificant data are indicated with NS. All of the computed $\Delta ATP(F_{Venus}/F_{CFP})$ are statistically significant changes or otherwise stated. Data are presented as scatterplot, bars (mean ± SEM), or as boxplots (if enough data are available), in which the yellow line corresponds to the mean, the whiskers to the 10th and 90th percentiles, the crosses (X) to the 5th and 95th percentiles, and the circles (•) the outliers (only shown when there are not enough data to compute the 5th and 95th percentiles). Number of experiments and analyzed cells are presented as number of independent experiments (n), number of cells. For analysis of rates, a linear function was fitted to the data. Oxygen consumption in brain tissue was simulated mathematically as detailed in *SI Appendix* using the affinity constant of cytochrome oxidase reported in (52).

ACKNOWLEDGMENTS. We thank Rodrigo Lerchundi for help with oxygen measurements, Juan Bolaños for bringing the Crabtree effect to our attention, and Karen Everett for critical reading of the manuscript. This work was partly funded by Fondecyt Grants 1160317 (to L.F.B.) and 3160131 (to I.R.), and the Deutsche Forschungsgemeinschaft (J.W.D.). The Centro de Estudios Científicos is supported by the Chilean Government through the Centers of Excellence Basal Financing Program of Comisión Nacional de Investigación Científica y Tecnológica-Chile.

1. Nicholls DG, Ferguson SJ (2013) *Bioenergetics* (Academic, London).
2. Pellerin L, Magistretti PJ (1994) Glutamate uptake into astrocytes stimulates aerobic glycolysis: A mechanism coupling neuronal activity to glucose utilization. *Proc Natl Acad Sci USA* 91:10625–10629.
3. Bittner CX, et al. (2011) Fast and reversible stimulation of astrocytic glycolysis by K+ and a delayed and persistent effect of glutamate. *J Neurosci* 31:4709–4713.
4. Imamura H, et al. (2009) Visualization of ATP levels inside single living cells with fluorescence resonance energy transfer-based genetically encoded indicators. *Proc Natl Acad Sci USA* 106:15651–15656.
5. Mamczur P, et al. (2015) Astrocyte-neuron crosstalk regulates the expression and subcellular localization of carbohydrate metabolism enzymes. *Glia* 63:328–340.
6. Hasel P, et al. (2017) Neurons and neuronal activity control gene expression in astrocytes to regulate their development and metabolism. *Nat Commun* 8:15132.
7. Fröhlich F, Bazhenov M, Iragui-Madoz V, Sejnowski TJ (2008) Potassium dynamics in the epileptic cortex: New insights on an old topic. *Neuroscientist* 14:422–433.
8. Ruminot I, et al. (2011) NBCe1 mediates the acute stimulation of astrocytic glycolysis by extracellular K+. *J Neurosci* 31:14264–14271.
9. Theparambil SM, Weber T, Schmälzle J, Ruminot I, Deitmer JW (2016) Proton fall or bicarbonate rise: Glycolytic rate in mouse astrocytes is paved by intracellular alkalinization. *J Biol Chem* 291:19108–19117.
10. Ruminot I, Schmalzle J, Leyton B, Barros LF, Deitmer JW (2017) Tight coupling of astrocyte energy metabolism to synaptic activity revealed by genetically encoded FRET nanosensors in hippocampal tissue. *J Cereb Blood Flow Metab*, 10.1177/0271678X17737012.
11. Chance B, Williams GR, Holmes WF, Higgins J (1955) Respiratory enzymes in oxidative phosphorylation. V. A mechanism for oxidative phosphorylation. *J Biol Chem* 217:439–451.
12. Kadenbach B, Ramzan R, Wen L, Vogt S (2010) New extension of the Mitchell theory for oxidative phosphorylation in mitochondria of living organisms. *Biochim Biophys Acta* 1800:205–212.
13. Crabtree HG (1929) Observations on the carbohydrate metabolism of tumours. *Biochem J* 23:536–545.
14. Ibsen KH (1961) The Crabtree effect: A review. *Cancer Res* 21:829–841.
15. Diaz-Ruiz R, Rigoulet M, Devin A (2011) The Warburg and Crabtree effects: On the origin of cancer cell energy metabolism and of yeast glucose repression. *Biochim Biophys Acta* 1807:568–576.
16. Fox PT, Raichle ME, Mintun MA, Dence C (1988) Nonoxidative glucose consumption during focal physiologic neural activity. *Science* 241:462–464.
17. Madsen PL, et al. (1995) Persistent resetting of the cerebral oxygen/glucose uptake ratio by brain activation: Evidence obtained with the Kety-Schmidt technique. *J Cereb Blood Flow Metab* 15:485–491.
18. Goyal MS, Hawrylycz M, Miller JA, Snyder AZ, Raichle ME (2014) Aerobic glycolysis in the human brain is associated with development and neotenous gene expression. *Cell Metab* 19:49–57.

19. Goyal MS, et al. (2017) Loss of brain aerobic glycolysis in normal human aging. *Cell Metab* 26:353–360.e3.
20. Vlassenko AG, et al. (2010) Spatial correlation between brain aerobic glycolysis and amyloid-β (Aβ) deposition. *Proc Natl Acad Sci USA* 107:17763–17767.
21. Chesler M, Kraig RP (1989) Intracellular pH transients of mammalian astrocytes. *J Neurosci* 9:2011–2019.
22. Deitmer JW, Szatkowski M (1990) Membrane potential dependence of intracellular pH regulation by identified glial cells in the leech central nervous system. *J Physiol* 421:617–631.
23. Pappas CA, Ransom BR (1994) Depolarization-induced alkalinization (DIA) in rat hippocampal astrocytes. *J Neurophysiol* 72:2816–2826.
24. Brookes N, Turner RJ (1994) K(+)-induced alkalinization in mouse cerebral astrocytes mediated by reversal of electrogenic Na(+)-HCO3- cotransport. *Am J Physiol* 267: C1633–C1640.
25. Jeneson JAL, et al. (2009) Magnitude and control of mitochondrial sensitivity to ADP. *Am J Physiol Endocrinol Metab* 297:E774–E784.
26. Herrero-Mendez A, et al. (2009) The bioenergetic and antioxidant status of neurons is controlled by continuous degradation of a key glycolytic enzyme by APC/C-Cdh1. *Nat Cell Biol* 11:747–752.
27. Almeida A, Almeida J, Bolaños JP, Moncada S (2001) Different responses of astrocytes and neurons to nitric oxide: The role of glycolytically generated ATP in astrocyte protection. *Proc Natl Acad Sci USA* 98:15294–15299.
28. Supplie LM, et al. (2017) Respiration-deficient astrocytes survive as glycolytic cells in vivo. *J Neurosci* 37:4231–4242.
29. Lopez-Fabuel I, et al. (2016) Complex I assembly into supercomplexes determines differential mitochondrial ROS production in neurons and astrocytes. *Proc Natl Acad Sci USA* 113:13063–13068.
30. Hagman A, Säll T, Compagno C, Piskur J (2013) Yeast "make-accumulate-consume" life strategy evolved as a multi-step process that predates the whole genome duplication. *PLoS One* 8:e68734.
31. Almeida A, Moncada S, Bolaños JP (2004) Nitric oxide switches on glycolysis through the AMP protein kinase and 6-phosphofructo-2-kinase pathway. *Nat Cell Biol* 6:45–51.
32. San Martín A, Arce-Molina R, Galaz A, Pérez-Guerra G, Barros LF (2017) Nanomolar nitric oxide concentrations quickly and reversibly modulate astrocytic energy metabolism. *J Biol Chem* 292:9432–9438.
33. Lebon V, et al. (2002) Astroglial contribution to brain energy metabolism in humans revealed by 13C nuclear magnetic resonance spectroscopy: Elucidation of the dominant pathway for neurotransmitter glutamate repletion and measurement of astrocytic oxidative metabolism. *J Neurosci* 22:1523–1531.
34. Blüml S, Moreno-Torres A, Shic F, Nguy C-H, Ross BD (2002) Tricarboxylic acid cycle of glia in the in vivo human brain. *NMR Biomed* 15:1–5.
35. Oz G, et al. (2004) Neuroglial metabolism in the awake rat brain: CO2 fixation increases with brain activity. *J Neurosci* 24:11273–11279.
36. Ebert D, Haller RG, Walton ME (2003) Energy contribution of octanoate to intact rat brain metabolism measured by 13C nuclear magnetic resonance spectroscopy. *J Neurosci* 23:5928–5935.
37. Weber B, Barros LF (2015) The astrocyte: Powerhouse and recycling center. *Cold Spring Harb Perspect Biol* 7:a020396.
38. Lerchundi R, et al. (2015) NH4(+) triggers the release of astrocytic lactate via mitochondrial pyruvate shunting. *Proc Natl Acad Sci USA* 112:11090–11095.
39. Buxton RB, Frank LR (1997) A model for the coupling between cerebral blood flow and oxygen metabolism during neural stimulation. *J Cereb Blood Flow Metab* 17: 64–72.
40. Devor A, et al. (2011) "Overshoot" of O_2 is required to maintain baseline tissue oxygenation at locations distal to blood vessels. *J Neurosci* 31:13676–13681.
41. Niven JE, Laughlin SB (2008) Energy limitation as a selective pressure on the evolution of sensory systems. *J Exp Biol* 211:1792–1804.
42. Suzuki A, et al. (2011) Astrocyte-neuron lactate transport is required for long-term memory formation. *Cell* 144:810–823.
43. Gawenis LR, et al. (2007) Colonic anion secretory defects and metabolic acidosis in mice lacking the NBC1 Na+/HCO3- cotransporter. *J Biol Chem* 282:9042–9052.
44. Yamada K, et al. (2001) Protective role of ATP-sensitive potassium channels in hypoxia-induced generalized seizure. *Science* 292:1543–1546.
45. Sussman CR, et al. (2009) Cloning, localization, and functional expression of the electrogenic Na+ bicarbonate cotransporter (NBCe1) from zebrafish. *Am J Physiol Cell Physiol* 297:C865–C875.
46. Takanaga H, Chaudhuri B, Frommer WB (2008) GLUT1 and GLUT9 as major contributors to glucose influx in HepG2 cells identified by a high sensitivity intramolecular FRET glucose sensor. *Biochim Biophys Acta* 1778:1091–1099.
47. San Martín A, et al. (2014) Imaging mitochondrial flux in single cells with a FRET sensor for pyruvate. *PLoS One* 9:e85780.
48. Schneider J, et al. (2015) A reliable model for gamma oscillations in hippocampal tissue. *J Neurosci Res* 93:1067–1078.
49. Stoppini L, Buchs PA, Muller D (1991) A simple method for organotypic cultures of nervous tissue. *J Neurosci Methods* 37:173–182.
50. Inoue M, Fujishiro N, Imanaga I, Sakamoto Y (2002) Role of ATP decrease in secretion induced by mitochondrial dysfunction in Guinea-pig adrenal chromaffin cells. *J Physiol* 539:145–155.
51. Magistretti PJ, Chatton J-Y (2005) Relationship between L-glutamate-regulated intracellular Na+ dynamics and ATP hydrolysis in astrocytes. *J Neural Transm (Vienna)* 112:77–85.
52. Brunori M, Antonini G, Malatesta F, Sarti P, Wilson MT (1988) Structure and function of cytochrome oxidase: A second look. *Adv Inorg Biochem* 7:93–153.